

Geophysical Research Letters

RESEARCH LETTER

10.1029/2018GL081299

Key Points:

- Failure in Etna basalt occurred through contraction localization, and then shear and dilation localization, consistent with geophysical observations
- Shear and volumetric strain localized into a protofault zone preceding 50% failure stress, and macroscopic yielding
- The precursors to volcanic flank eruptions may include a transition from contraction to dilation

Supporting Information:

- Supporting Information S1

Correspondence to:

J. A. McBeck,
j.a.mcbeck@geo.uio.no

Citation:

McBeck, J. A., Cordonnier, B., Vinciguerra, S., & Renard, F. (2019). Volumetric and shear strain localization in Mt. Etna basalt. *Geophysical Research Letters*, *46*, 2425–2433. <https://doi.org/10.1029/2018GL081299>

Received 12 NOV 2018

Accepted 13 FEB 2019

Accepted article online 19 FEB 2019

Published online 4 MAR 2019

Volumetric and Shear Strain Localization in Mt. Etna Basalt

Jessica A. McBeck¹ , Benoît Cordonnier¹, Sergio Vinciguerra² , and François Renard^{1,3} 

¹Physics of Geological Processes, The Njord Centre, Department of Geosciences, University of Oslo, Oslo, Norway,

²Department of Earth Sciences, University of Turin, Turin, Italy, ³Université Grenoble Alpes, Université Savoie Mont Blanc, CNRS, IRD, IFSTTAR, ISTERRE, Grenoble, France

Abstract To examine the impact of preexisting weaknesses on fracture coalescence during volcanic edifice deformation, we triaxially compressed Mount Etna basalt while acquiring in situ dynamic X-ray microtomograms and calculated the internal strain tensor fields using image correlation. Contraction localization preceded dilation and shear strain localization into the protofault zone. This onset of strain localization preceded macroscopic yielding and coincided with increases in the magnitude and volume of rock experiencing dilation, and spatial clustering of the strain populations. The exploitation of weaknesses by propagating fractures enabled the dominant shear strain to switch senses as propagating fractures lengthened along 30–60° from σ_1 . Scanning electron microscopy images reveal pore-emanated fractures, and fractures linking pores. These experiments provide evidence of internal contraction preceding dilation and shear, consistent with inferences from field and laboratory observations. The transition from contraction to dilation may provide a precursory signal of volcanic flank eruption.

Plain language summary Directly observing how rocks break at seismogenic depths in natural settings is at present impossible. Here we used X-ray imaging techniques to view deforming, and then breaking, basaltic rocks at stress conditions equivalent to the flanks of the upper part of the Mount Etna volcano. We tracked how preexisting weaknesses, including pores and fractures produced during the fast cooling of the lava, controlled the growth and coalescence of new fractures and faults. At 50% of the stress at failure, shear and dilative strains began to concentrate in the volume that eventually developed the largest connected fracture network. The localization of contractive strains preceded this shear and dilation localization. These data sets provide observations of fracture growth within Etna basalt that previous studies could only infer, and thus constraints on how the volcanic edifice deforms under magmatic and tectonic stresses and eventually ruptures in flank eruptions.

1. Introduction

Understanding the geomechanical response of basalt is fundamental to predicting the deformation and stability of volcanic edifices under magmatic pressurization. The evolving mechanical properties of the edifice control magma emplacement and storage, and the deformation mechanisms that enable flank eruption (e.g., Aloisi et al., 2011; Famin & Michon, 2010; Privitera et al., 2012). Field observations and geophysical monitoring reveal perturbations of mechanical properties of volcanic systems preceding eruptions (e.g., Brenguier et al., 2008; Carbone et al., 2014; Hautmann et al., 2010; Ratdomopurbo & Poupinet, 1995). In particular, gravity data acquired at Mt. Etna indicate alternating decreases and increases in density in the interval between the 1991–1993 and 2001 flank eruptions, with the most significant mass redistributions at shallower depths (Carbone et al., 2003a, 2003b, 2009, 2014). These observations indicate that accelerating rates of microfracture development may have driven the observed gravity decreases, rather than deeper magma emplacement (e.g., Carbone et al., 2014). The observed gravity increases may have arisen from shallower magma emplacement (e.g., Carbone et al., 2014). However, local contraction of the host rock may also increase gravity. Analyses of GPS displacements provide additional evidence of contraction preceding volcanic activity on Mt. Etna (Bonforte & Puglisi, 2003). In particular, GPS surveys on Mt. Etna identified an E-W and NW-SE contraction of the summit craters area and upper section of the NE rift preceding volcanic activity in October 1995 on the order of $2 \mu\epsilon$ (Bonforte & Puglisi, 2003).

Rock deformation laboratory experiments provide direct observations of changes in physical properties of volcanic rocks, as they are deformed toward failure that we can only infer from depth- and time-averaged

field observations. Unlike field observations, these analyses are not encumbered by the intrusion of solidifying magma, and so they can isolate the response of the host rock from the dynamics of the magma. Experimental studies find that the deformation of Etna basalt produces changes in seismic velocities, elastic anisotropy, elastic moduli, acoustic emission output, and permeability (e.g., Becker et al., 2007; Benson et al., 2007; Faoro et al., 2013; Fortin et al., 2011; Heap et al., 2009; Stanchits et al., 2006; Vinciguerra et al., 2005). In particular, seismic velocities, acoustic emission sources, and microstructural observations reveal volume decreases (contraction) in basalt under deviatoric loading at low effective pressures (Benson et al., 2007; Fortin et al., 2011; Zhu et al., 2016). These studies attribute the volume decreases to the closure of preexisting pore space. With increasing deviatoric loading, these studies observed volume increases that they interpret as newly nucleating and propagating fractures oriented parallel to the main compressive stress, σ_1 .

To examine how preexisting weaknesses influence the propagation, arrest, and coalescence of fractures in deforming volcanic edifices, we triaxially compressed Etna basalt while acquiring in situ tomograms. Through segmentation of the tomograms into solid rock and fractures/pores, we directly observed the evolving geometry of fracture networks, including their orientation. Through digital volume correlation (DVC), we tracked the magnitude and spatial localization of the volumetric and distortional strain components. These data provide in situ observations of the geometry and orientation of developing fractures during triaxial compression, their interaction with preexisting pores, and the magnitude and localization of strain they accommodate that previous studies could only infer. These observations provide insights into a potential precursory mechanism to volcanic edifice rupture that can be detected with geophysical monitoring: the transition from contraction-dominated to dilation-dominated deformation.

2. Methods

Mt. Etna basalt is a porphyritic intermediate alkali basalt that underwent rapid cooling and degassing (Heap et al., 2009). This rapid cooling rate and degassing produced macropores and micropores (e.g., Benson et al., 2007; Zhu et al., 2016), and thermal-induced fractures that generally are isotopically distributed without a preferred orientation (Vinciguerra et al., 2005).

We triaxially compressed two cores of Etna basalt using the X-ray transparent Hades deformation apparatus (Renard et al., 2016) installed at microtomography beamline ID19 at ESRF. We cored two 10-mm-long and 3.7-mm-diameter cylinders from a block of basalt from the quarry described by Heap et al. (2009), using a diamond drill bit with subsequent sandpaper correction. The cores had initial porosities of 3%, measured from the tomograms.

We subjected the cores to 10-MPa confining stress and then increased the axial stress in steps until the basalt failed, with larger stress steps (5 MPa) far from failure and smaller stress steps (1 MPa) closer to failure (Figure 1). This confining stress represents an upper crustal lithostatic load (0.3-km depth) of basaltic rock. We applied the axial stress parallel to the long axis of the cores. We performed the experiments at room temperature, without fluid. After each stress step, we acquired tomograms inside the apparatus at $6.5 \mu\text{m}/\text{voxel}$ within 90 s. Each stress step and scan acquisition required 3–5 min.

The voxel values of the tomograms reflect differences in electron density and atomic number. Segmentation of the voxel values into voxels dominated by air or by rock provided 3-D distributions of preexisting open pores and microfractures. We identified the segmentation threshold from histograms of voxel values, after applying several image processing techniques (e.g., Renard et al., 2018). This segmentation captures deformation that produces changes in local density.

To detect shear and volumetric deformation, we employed DVC using TomoWarp2 (Tudisco et al., 2017). By matching voxel constellations across sequential tomograms, DVC produces displacement fields of the deformation that occurred between tomogram acquisitions. From these fields, we calculated the divergence and curl fields. We tracked the positive and negative divergence and curl in order to capture the dilation, contraction, and right-lateral and left-lateral shear strain (Text S1 in the supporting information). Following previous approaches to DVC analysis (McBeck et al., 2018), we calculated incremental displacement fields between 10 tomogram pairs that are separated by approximately constant changes in applied axial strain, $\Delta\varepsilon_{zz}^M$. To account for small differences in $\Delta\varepsilon_{zz}^M$ between each pair, we normalized the calculated divergence and curl values by $\Delta\varepsilon_{zz}^M$.

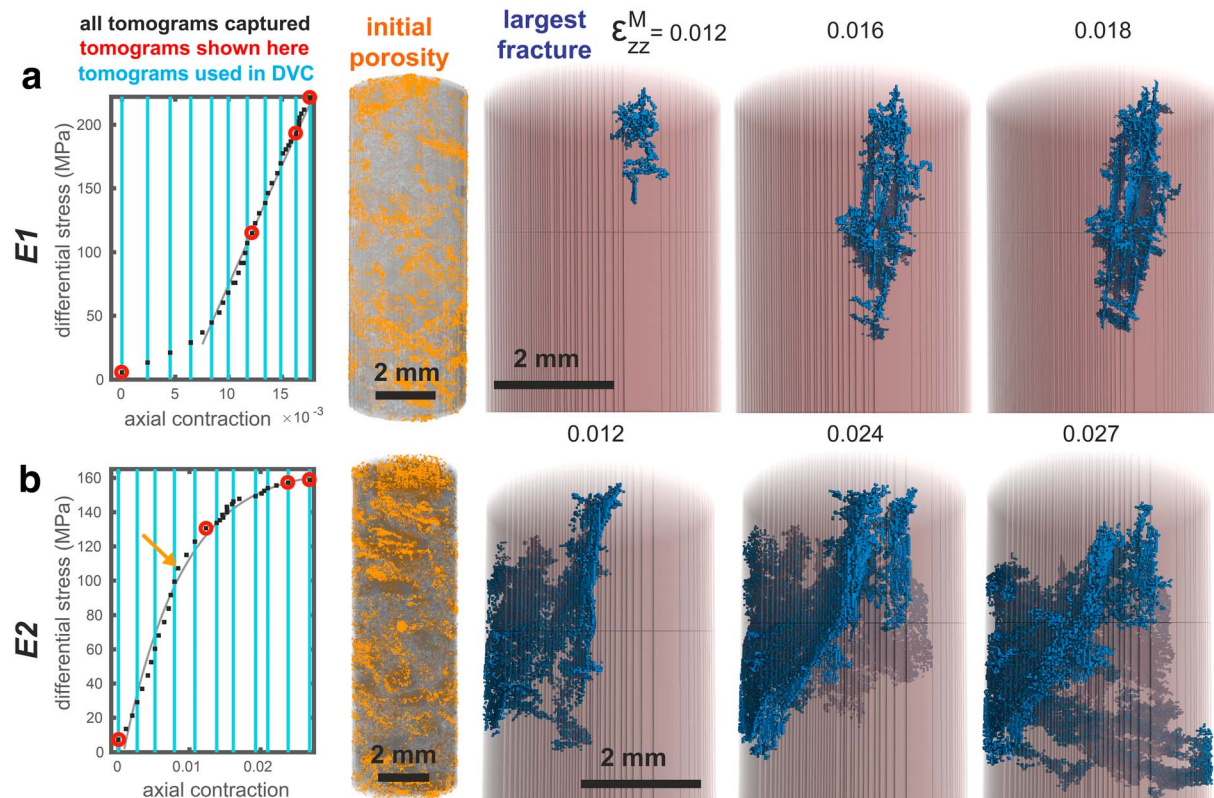


Figure 1. Axial strain versus differential stress for all captured tomograms (black dots) and the tomograms shown here (red circles) for experiments E1 (a) and E2 (b). Blue lines indicate tomogram pairs used in the digital volume correlation (DVC) analysis. Gray lines show best fit functions to stress-strain relationships. (b) Orange arrow shows yield point. Segmentation of preexisting pores and fractures (yellow) and the largest continuous fracture network (blue) in experiment steps.

To quantify the spatial localization of the incremental strain populations, we used the coefficient Moran's I (Moran, 1948) to characterize spatial clustering (e.g., Thompson et al., 2018; Zhang & Lin, 2016). When Moran's I is positive, populations are spatially correlated with each other so that members of the population with similar values are located nearby to each other. This spatial correlation statistic is particularly suitable for determining whether data are clustered, regardless of whether high or low values are clustered. Text S2 describes additional details of this calculation.

To examine the interaction of propagating fractures and preexisting pores, we performed scanning electron microscopy (SEM) on cores recovered postdeformation. After macroscopic failure, we impregnated the core with epoxy to prevent ex situ damage. We cut the cores along a midsection vertical plane, polished the newly exposed surface, and coated the surface with 8 nm of carbon. We imaged the exposed surfaces using a Hitachi S5000 Scanning Electron Microscope at the University of Oslo with a voltage of 15 kV.

3. Results

3.1. Linking Macroscopic Mechanical Behavior to Fracture Coalescence

The macroscopic axial strain and differential stress relationships of the two experiments differ from each other, although the experimental conditions and rock cores were as identical as possible (Figure 1). The axial strain-differential stress relationship of experiment E1 forms a quasi-linear relationship following an early loading stage, whereas an exponential function fits the stress-strain relationship of experiment E2. In experiment E1, the early shallow slope of the differential stress-strain curve coincides with the straightening of the core to a more parallel orientation to σ_1 (Movie S1). In experiment E2, such a significant adjustment of the core inside the rig did not occur (Movie S2). The observed increase in the apparent elastic modulus may also arise in part from preexisting pores closing.

The experiments have different evolutions of differential stress and axial strain because experiment E1 failed suddenly without a distinctive yielding phase, whereas experiment E2 hosted a yielding phase in which the strain-stress curve shallowed. Segmentation of the tomograms into voids and rock provides insights into these differences in macroscopic behavior. The largest connected fracture network developed near the upper piston and then propagated downward at oblique angles to σ_1 (vertical) in both experiments (Figure 1). In experiment E1, the largest fracture network trends near 60° from σ_1 , consistent with the orientation of the highest Coulomb stress (τ/σ_n), and are more steeply oriented than 60° in experiment E2. The volume and geometry of the largest fracture network remained relatively similar in the final three tomograms preceding failure in experiment E1 (Movie S3). In contrast, this network continued to grow in the final three tomograms of experiment E2 (Movie S4; Figure 1b). The continued growth of the largest fracture network in experiment E2 indicates that fracture development was able to effectively accommodate the applied differential stress in this final stage preceding failure. The lack of significant fracture network growth observed in experiment E1 indicates that this growth was not able to accommodate loading as effectively as in experiment E2. This ineffectiveness then promoted macroscopic failure in a sudden stress drop rather than continued yielding via microfracture growth.

3.2. Spatial Distribution of Deformation

The evolving spatial distribution of the incremental strain values calculated with DVC provide criteria to recognize the onset of strain localization into the protofault zone that ultimately hosted the largest connected fracture network preceding macroscopic failure. We identify this localization onset using high dilatational and shear strain values (>90th percentile; Figure 2; Movies S3 and S4). The porosity and confining stress of these experiments suggest that failure occurs through opening and shear, and not contractive compaction band formation (e.g., Mair et al., 2002; Schultz et al., 2010) or shear-enhanced compaction (e.g., Zhu et al., 2016). Consequently, we use high values of dilation and shear strain (that exceed the >90th percentile) to recognize this localization onset.

The onset occurred near 50% of the differential stress at failure in both experiments (Figure 2; Movies S5 and S6), or near 0.012 and 0.0075 macroscopic axial strain in experiments E1 and E2, respectively. This onset preceded the macroscopic yielding phase recognized in experiment E2, near 0.01 macroscopic axial strain (orange arrow in Figure 1b). This onset followed the concentration of high contractive values (negative divergence) into more clustered spatial distributions (Figure 2; Movies S5 and S6). Whereas high shear strain and dilation localized into the protofault zone, high contractive strain values clustered within other portions of the core during the onset (Figure 2b). This early onset of failure may have occurred preceding macroscopic yielding, and near 50% of the differential stress at failure, because preexisting pores and fractures promoted fracture growth and linkage at these differential stresses without yet signaling a decrease of effective stiffness in the stress-strain curve.

Differences in the spatial distribution of high contraction also informs the absence of a clear yielding phase in experiment E1. Whereas concentrated contraction within the fault zone accommodated loading in experiment E2, contraction did not localize within the fault zone in experiment E1. This concentrated contraction may aid the ability of the core to axially contract without failing macroscopically.

Tracking the mean and standard deviation of the divergence and curl populations calculated in the DVC analysis indicates that increases in the magnitude of dilation, but not the other strain components, characterizes the localization onset (Figure 3a). Tracking the volume of material experiencing dilation or contraction, and left- or right-lateral shear strain, indicates that the onset coincided with changes in the dominant volumetric strain sense from contraction to dilation, and differing senses of shear (Figure 3b). Preceding the onset, 65–90% of the core hosted contraction, and after this onset, only 15–25% of the core hosted contraction. Moreover, preceding the onset, the mean of the dilatational strains was 70–80% of the contractive strains. And following the onset, the mean of the contractive strains was 15–35% of the dilatative strains.

Following the onset, the sense of shear strain changed twice in each experiment, at 0.01 and 0.019 (experiment E1 and 0.01 and 0.021 (experiment E2) axial strain. Preexisting weaknesses in the basalt cores may have assisted this fluctuation of shear sense by allowing growing and coalescing fractures to readily exploit weaknesses. Segmentation of the tomograms indicates that the preexisting weaknesses were distributed in

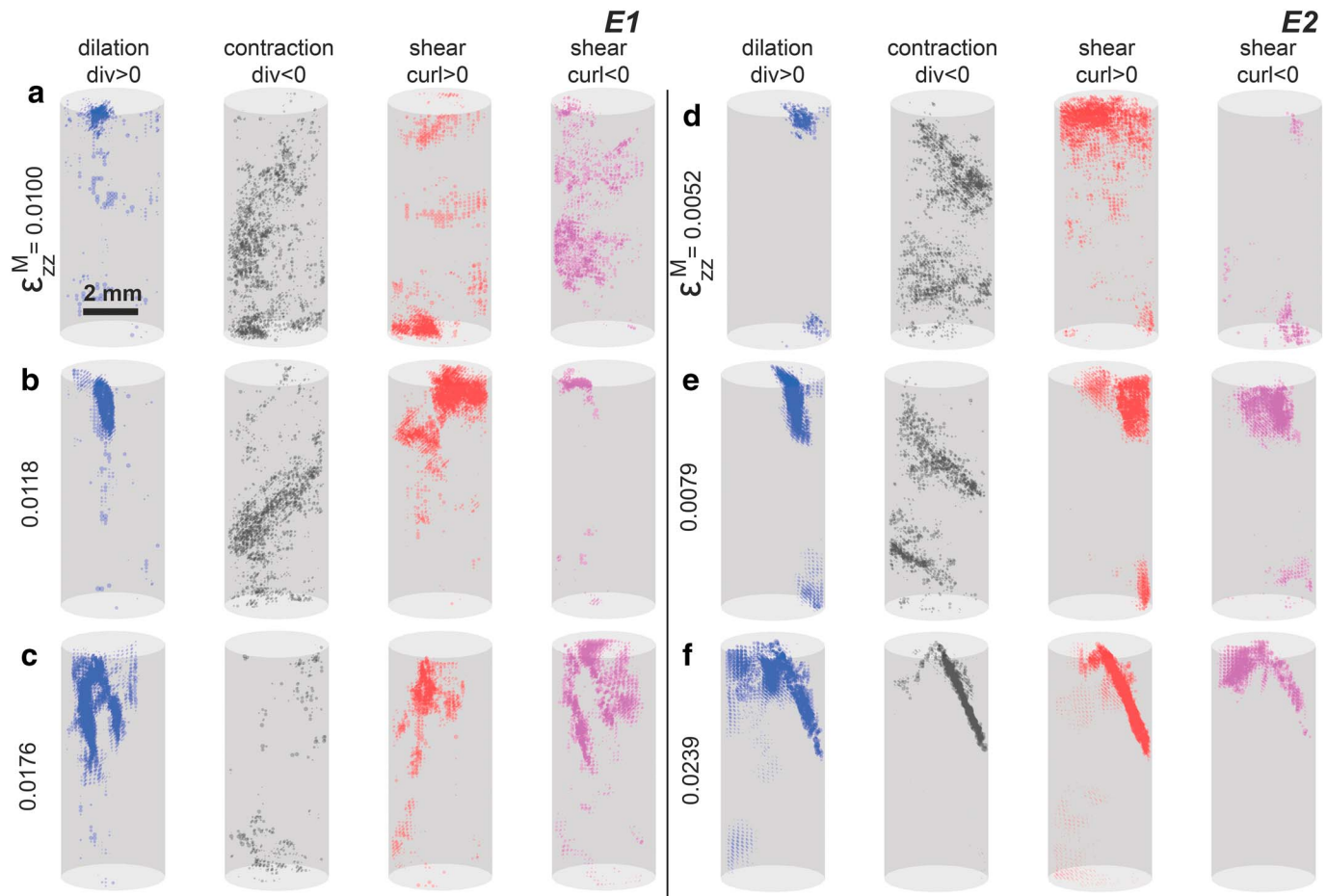


Figure 2. Evolution of spatial distribution of high incremental strains (>90th percentile) in experiments E1 (a–c) and E2 (d–f). Location of rock experiencing high dilation, contraction, right-lateral shear, and left-lateral shear shown with symbols with sizes proportional to their magnitude. (b and e) Digital volume correlation increments that capture the strain localization onset within the protofault zones.

clusters throughout the cores (Figure 1). This clustering likely enhanced the stress-concentrating influence of these weaknesses and so helped drive fracture development toward and near them.

The consistently positive Moran's I values indicate that the strains were clustered throughout deformation, with similar strain magnitudes located near to each other (Figure 3c). In experiment E1, a distinct increase in the clustering of strains coincided with the localization onset. In experiment E2, such an increase in clustering near the onset only occurred in the contractive strain values. In contrast, the clustering of the shear strain and dilation populations decreased slightly near the onset preceding macroscopic failure. Qualitative observations of the spatial distributions of the high strain values match the evolution of Moran's I (Text S3).

3.3. Interaction of Preexisting Weaknesses and Coalescing Fractures

To examine how propagating fractures interact with preexisting pores and microfractures, we track the preferred alignment of voids, including growing or collapsing pores, and propagating and coalescing fractures. To differentiate between pores and fractures, we consider voids with anisotropies above the mean plus one standard deviation of the population as dominated by fractures, and voids below this threshold are dominated by pores (Figure S1). Throughout loading in both experiments, pores were oriented more isotropically than fractures (Figure S2). The preferred orientation of fractures shifted from perpendicular to σ_1 at the onset of loading, toward 30–60° from σ_1 after only 5–10 MPa of applied differential stress, consistent with the orientation of the maximum Coulomb stress. Following this shift toward orientations oblique to σ_1 , the preferred orientation of fractures remained consistent until macroscopic failure.

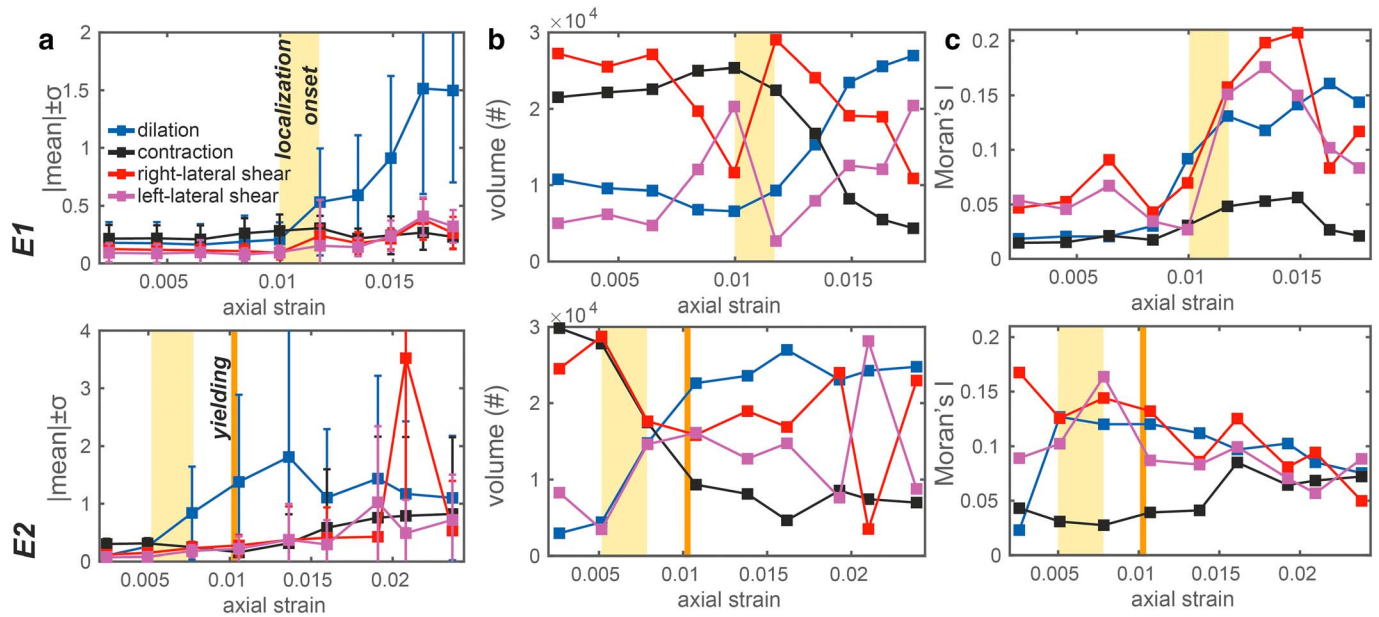


Figure 3. Evolution of magnitude, volume, and clustering of strains in experiment E1 (top) and E2 (bottom). (a) Mean \pm one standard deviation of the positive and negative divergence and curl. Orange lines show the yield point of experiment E2. (b) Volume experiencing strain components as the number of values. (c) Spatial correlation of components: Moran's I . Yellow bars show the time of localization onset.

The number of pores and fractures remained similar throughout loading (28,500 to 29,700 and 22,800 to 21,700 in experiments E1 and E2, respectively). This consistency suggests that preexisting pores and fractures grew throughout loading but few new fractures nucleated. Some new fractures may have nucleated, but as other fractures and pores coalesced, the total number of voids remained within 3–4% of each other. This behavior highlights how the developing fracture network exploited the preexisting weaknesses.

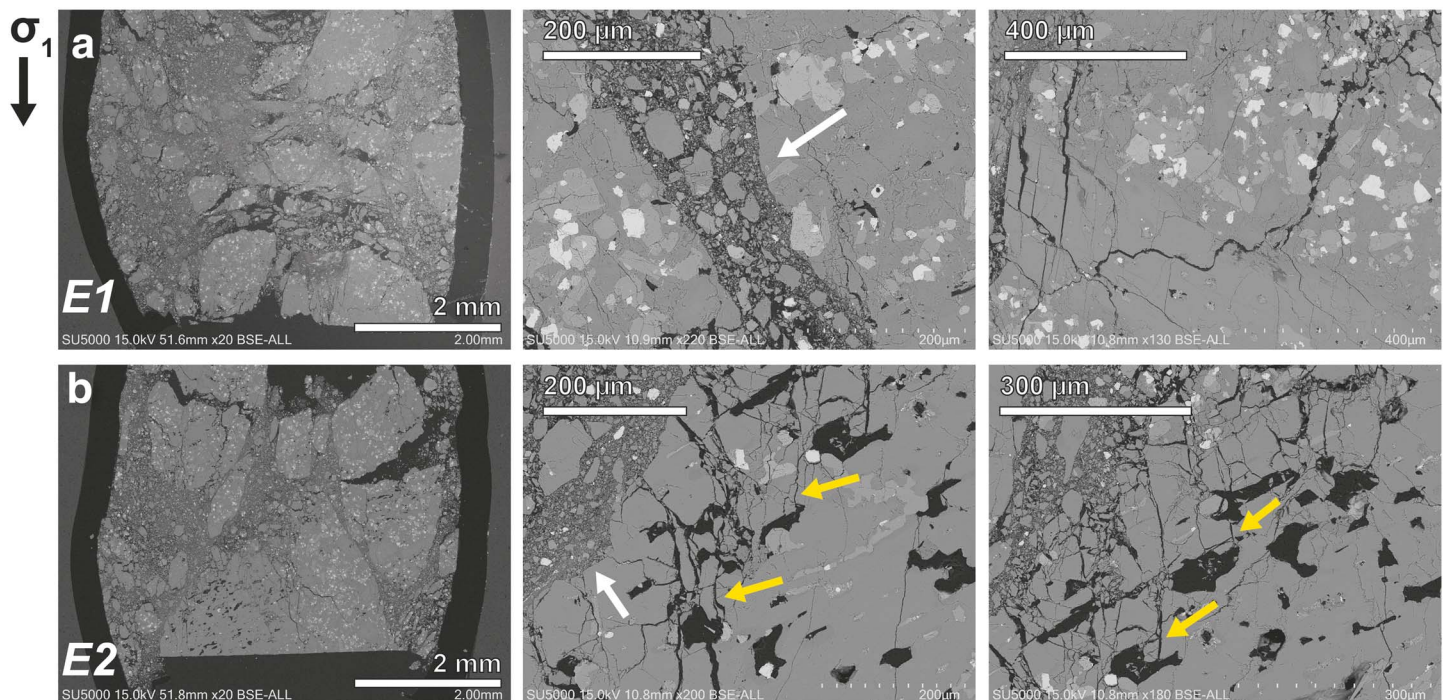


Figure 4. Scanning electron microscopy images of experiments E1 (a) and E2 (b). Thicker fracture zones are filled with crushed rock (white arrows). Thinner fractures lack this thick fault gouge and often connect preexisting neighboring pores (yellow arrows).

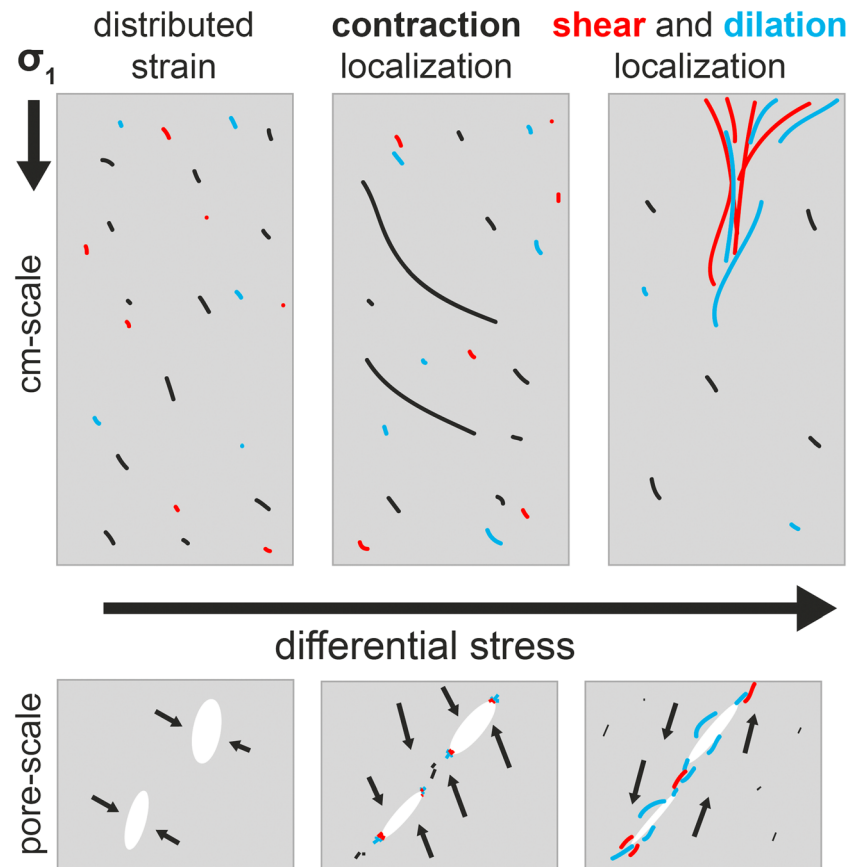


Figure 5. Schematic representation of strain localization at the centimeter and pore scales. Localized higher strain magnitudes shown in black (contraction), blue (dilation), and red (shear strain). Arrows in pore-scale sketches show direction of host rock movement.

SEM imaging of the cores postfailure reveal additional insights into how the preexisting weaknesses impacted fracture development. Thinner fractures connect nearby pores (Figure 4), highlighting the fracture-attracting influence of the pores. The thicker fault zones are filled with crushed rock fragments. Thinner fractures lack this thick fault gouge, likely because they have not hosted sufficient shear strain or contraction to comminute previously intact rock.

4. Discussion and Conclusions

Analysis of X-ray microtomography scans provide detailed insights into the strain localization process in rock with pervasive preexisting weaknesses. The evolving spatial distribution of strains indicates that high dilation and shear strains (>90th percentile) began to concentrate within the region that hosted the largest fracture network near 50% of the failure stress (Figure 2; Movies S5 and S6), preceding macroscopic yielding observed in the strain-stress relationship. The concentration of high contractive strains into other portions of the core preceded this onset (Figures 2b and 5). This contraction localization is consistent with previous experiments that observe increases in the seismic wave velocity parallel to σ_1 , and corresponding increases in seismic anisotropy, which have been linked to pores closing perpendicular to σ_1 (Benson et al., 2007; Stanchits et al., 2006) and observations of local contraction from GPS displacements (Bonforte & Puglisi, 2003). The observed contraction also suggests that local gravity increases in the shallow depths of Mt. Etna between flank eruptions (e.g., Carbone et al., 2014) may arise not only from magma emplacement but also from volumetric contraction of the host rock. Furthermore, we observe local dilation following the contraction-dominated phase, consistent with local gravity decreases observed at Mt. Etna, interpreted as dilatant microfracturing (e.g., Carbone et al., 2014). Our results provide quantitative support to this geophysical interpretation and show that contraction localization was a precursor to dilation and shear strain

localization into the protofault zone that hosted the largest fracture network. Time series of the strain invariants derived from GPS campaigns could provide additional evidence of a transition from volumetric contraction to dilation preceding flank eruption, such as analyses of areal strain evolutions (Bonforte & Puglisi, 2003). We provide histograms of the populations of the first invariant of the strain tensor and von Mises equivalent strain (Figure S3) to assist comparison of these strain evolutions with future field measurements.

Postmortem microstructural analyses of basalts deformed in triaxial tests suggest that pore-emanated fracturing can become the dominant mechanism of stress-induced damage leading to brittle faulting (Zhu et al., 2016). Similarly, our SEM images show thin fractures linking pores (Figure 4). Segmentation of the tomograms indicates that the fractures developed a preferred orientation near 30–60° from σ_1 after only 5–10 MPa applied σ_D (Figure S2). This analysis also indicates that the total number of individual fractures and pores remained consistent throughout deformation, suggesting that growing fractures exploited preexisting weaknesses rather than nucleating independently of these weaknesses. Whereas previous experimental studies on basalt inferred the vertical propagation of new fractures parallel to σ_1 (e.g., Zhu et al., 2016), we observed the lengthening of preexisting fractures 30–60° from σ_1 .

From our experimental observations, we infer that at the pore scale (Figure 5), initial loading closed some pores. Upon further loading, the volumes of rock between neighboring pores were also able to close, promoting shear and dilation near the tips of pores. Finally, fractures hosting shear and dilation near the top of the core coalesced as pore-emanated fractures began to link neighboring pores and fractures along orientations 30–60° from σ_1 . The magnitude of the mean internal dilation increased by larger percentages (~500%) than contraction or shear strain (~100%) from the onset of loading until macroscopic failure. The progression from contraction-dominated to dilation-dominated strain fields preceding failure, and preceding macroscopic yielding, suggests that this transition may be a precursor to volcanic flank eruption recognizable in geophysical observations.

Acknowledgments

Sanchez Technology built the deformation apparatus. Elodie Boller, Paul Tafforeau, and Alexander Rack provided advice on the tomography setup. Stephen Hall and Erika Tudisco provided advice on TomoWarp2. The Norwegian Research Council funded this work (Grant 250661). Beamtime was allocated at the European Synchrotron Radiation Facility (Long Term Proposal ES-295). Data storage was provided by UNINETT Sigma2 (project NS9073K). The X-ray tomography data are available (Renard, 2018). We thank Editor Carey and two anonymous reviewers for suggestions that improved the manuscript.

References

- Aloisi, M., Mattia, M., Monaco, C., & Pulvirenti, F. (2011). Magma, faults, and gravitational loading at Mount Etna: The 2002–2003 eruptive period. *Journal of Geophysical Research*, *116*, B05203. <https://doi.org/10.1029/2010JB007909>
- Becker, K., Shapiro, S. A., Stanchits, S., Dresen, G., & Vinciguerra, S. (2007). Stress induced elastic anisotropy of the Etnean basalt: Theoretical and laboratory examination. *Geophysical Research Letters*, *34*, L11307. <https://doi.org/10.1029/2007GL030013>
- Benson, P. M., Thompson, B. D., Meredith, P. G., Vinciguerra, S., & Young, R. P. (2007). Imaging slow failure in triaxially deformed Etna basalt using 3D acoustic-emission location and X-ray computed tomography. *Geophysical Research Letters*, *34*, L03303. <https://doi.org/10.1029/2006GL028721>
- Bonforte, A., & Puglisi, G. (2003). Magma uprising and flank dynamics on Mount Etna volcano, studied using GPS data (1994–1995). *Journal of Geophysical Research*, *108*(B3), 2153. <https://doi.org/10.1029/2002JB001845>
- Brenguier, F., Shapiro, N. M., Campillo, M., Ferrazzini, V., Duputel, Z., Coutant, O., & Nercessian, A. (2008). Towards forecasting volcanic eruptions using seismic noise. *Nature Geoscience*, *1*(2), 126–130. <https://doi.org/10.1038/ngeo104>
- Carbone, D., Aloisi, M., Vinciguerra, S., & Puglisi, G. (2014). Stress, strain and mass changes at Mt. Etna during the period between the 1993–94 and 2001 flank eruptions. *Earth-Science Reviews*, *138*, 454–468. <https://doi.org/10.1016/j.earscirev.2014.07.004>
- Carbone, D., Budetta, G., & Greco, F. (2003a). Bulk processes prior to the 2001 Mount Etna eruption, highlighted through microgravity studies. *Journal of Geophysical Research*, *108*(B12), 2556. <https://doi.org/10.1029/2003JB002542>
- Carbone, D., Budetta, G., & Greco, F. (2003b). Possible mechanisms of magma redistribution under Mt Etna during the 1994–1999 period detected through microgravity measurements. *Geophysical Journal International*, *153*(1), 187–200. <https://doi.org/10.1046/j.1365-246X.2003.01901.x>
- Carbone, D., D'Amico, S., Musumeci, C., & Greco, F. (2009). Comparison between the 1994–2006 seismic and gravity data from Mt. Etna: New insight into the long-term behavior of a complex volcano. *Earth and Planetary Science Letters*, *279*(3–4), 282–292. <https://doi.org/10.1016/j.epsl.2009.01.007>
- Famin, V., & Michon, L. (2010). Volcano destabilization by magma injections in a detachment. *Geology*, *38*(3), 219–222. <https://doi.org/10.1130/G30717.1>
- Faoro, I., Vinciguerra, S., Marone, C., Elsworth, D., & Schubnel, A. (2013). Linking permeability and mechanical damage for basalt from Mt Etna Volcano. *Geophysical Research Letters*, *40*, 2590–2595. <https://doi.org/10.1002/grl.50436>
- Fortin, J., Stanchits, S., Vinciguerra, S., & Dresen, G. (2011). Influence of thermal and mechanical cracks on permeability and elastic wave velocities in a basalt from Mt. Etna volcano subjected to elevated pressure. *Tectonophysics*, *503*(1–2), 60–74. <https://doi.org/10.1016/j.tecto.2010.09.028>
- Hautmann, S., Gottsmann, J., Camacho, A. G., Fournier, N., Sacks, I. S., & Sparks, R. S. J. (2010). Mass variations in response to magmatic stress changes at Soufrière Hills Volcano Montserrat (W.I.): Insights from 4-D gravity data. *Earth and Planetary Science Letters*, *290*(1–2), 83–89. <https://doi.org/10.1016/j.epsl.2009.12.004>
- Heap, M. J., Vinciguerra, S., & Meredith, P. (2009). The evolution of elastic moduli with increasing crack damage during cyclic stressing of a basalt from Mt. Etna volcano. *Tectonophysics*, *471*(1–2), 153–160. <https://doi.org/10.1016/j.tecto.2008.10.004>
- Mair, K., Elphick, S., & Main, I. (2002). Influence of confining pressure on the mechanical and structural evolution of laboratory deformation bands. *Geophysical Research Letters*, *29*(10), 1410. <https://doi.org/10.1029/2001GL013964>

- McBeck, J., Kobchenko, M., Hall, S., Tudisco, E., Cordonnier, B., Meakin, P., & Renard, F. (2018). Investigating the onset of strain localization within anisotropic shale using digital volume correlation of time-resolved X-ray microtomography images. *Journal of Geophysical Research: Solid Earth*, *123*, 7509–7528. <https://doi.org/10.1029/2018JB015676>
- Moran, P. A. (1948). The interpretation of statistical maps. *Journal of the Royal Statistical Society: Series B: Methodological*, *10*(2), 243–251. <https://doi.org/10.1111/j.2517-6161.1948.tb00012.x>
- Privitera, E., Bonanno, A., Gresta, S., Nunnari, G., & Puglisi, G. (2012). Triggering mechanisms of static stress on Mount Etna volcano. An application of the boundary element method. *Journal of Volcanology and Geothermal Research*, *245–246*, 149–158. <https://doi.org/10.1016/j.jvolgeores.2012.08.012>
- Ratdomopurbo, A., & Poupinet, G. (1995). Monitoring a temporal change of seismic velocity in a volcano: Application to the 1992 eruption of Mt. Merapi (Indonesia). *Geophysical Research Letters*, *22*(7), 775–778. <https://doi.org/10.1029/95GL00302>
- Renard, F. (2018). Volumetric and shear strain localization in Mt. Etna basalt [Data set]. Norstore. <https://doi.org/10.11582/2018.00036>
- Renard, F., Cordonnier, B., Dysthe, D., Boller, E., Tafforeau, P., & Rack, A. (2016). A deformation rig for synchrotron microtomography studies of geomaterials under conditions down to 10 km depth in the Earth. *Journal of Synchrotron Radiation*, *23*(4), 1030–1034. <https://doi.org/10.1107/S1600577516008730>
- Renard, F., Weiss, J., Mathiesen, J., Ben-Zion, Y., Kandula, N., & Cordonnier, B. (2018). Critical evolution of damage toward system-size failure in crystalline rock. *Journal of Geophysical Research: Solid Earth*, *123*, 1969–1986. <https://doi.org/10.1002/2017JB014964>
- Schultz, R. A., Okubo, C. H., & Fossen, H. (2010). Porosity and grain size controls on compaction band formation in Jurassic Navajo Sandstone. *Geophysical Research Letters*, *37*, L22306. <https://doi.org/10.1029/2010GL044909>
- Stanchits, S., Vinciguerra, S., & Dresen, G. (2006). Ultrasonic velocities, acoustic emission characteristics and crack damage of basalt and granite. *Pure and Applied Geophysics*, *163*(5–6), 975–994. <https://doi.org/10.1007/s00024-006-0059-5>
- Thompson, E. S., Saveyn, P., Declercq, M., Meert, J., Guida, V., Eads, C. D., et al. (2018). Characterisation of heterogeneity and spatial autocorrelation in phase separating mixtures using Moran's I. *Journal of Colloid and Interface Science*, *513*, 180–187. <https://doi.org/10.1016/j.jcis.2017.10.115>
- Tudisco, E., Andò, E., Cailletaud, R., & Hall, S. A. (2017). TomoWarp2: A local digital volume correlation code. *SoftwareX*, *6*, 267–270. <https://doi.org/10.1016/j.softx.2017.10.002>
- Vinciguerra, S., Trovato, C., Meredith, P. G., & Benson, P. M. (2005). Relating seismic velocities, thermal cracking and permeability in Mt. Etna and Iceland basalts. *International Journal of Rock Mechanics and Mining Sciences*, *42*(7–8), 900–910. <https://doi.org/10.1016/j.ijrmms.2005.05.022>
- Zhang, T., & Lin, G. (2016). On Moran's I coefficient under heterogeneity. *Computational Statistics & Data Analysis*, *95*, 83–94. <https://doi.org/10.1016/j.csda.2015.09.010>
- Zhu, W., Baud, P., Vinciguerra, S., & Wong, T. F. (2016). Micromechanics of brittle faulting and cataclastic flow in Mount Etna basalt. *Journal of Geophysical Research: Solid Earth*, *121*, 4268–4289. <https://doi.org/10.1002/2016JB012826>